ROYAL SOCIETY
OF CHEMISTRY

PAPER

Check for updates

Coal-based graphene derived from different coal ranks: exceptional sodium storage performance in sodium-ion batteries†

Lanhao Wang,[ab] Xiaodong Yu,[ab] Zhendong Jiang, [ID] *[cd] Xusheng Li[bc] and Chuanxiang Zhang [ID] [cd]

Coal is a premium carbon material precursor as anode materials for sodium-ion batteries (SIBs). Additionally, developing anode materials with large capacity and rapid charging performance is essential for the advancement of SIBs. Consequently, in this work, coal-based reduced graphene oxide (CrGO) was prepared as an anode materials for SIBs by a modified Hummers-high temperature thermal reduction method with different ranks of coal (coal-based graphite, CG) as a precursor. The CG prepared from higher-rank coal exhibits a higher degree of graphitization, and its graphene layers are easier to exfoliate. The unique microstructure of CrGO provides stability during the sodium storage process and exhibits fast ion capacitive adsorption behavior, enhancing reaction kinetics. CrGO, with an initial reversible capacity of up to 331 mA h g^{-1} at a current density of 0.03 A g^{-1}, achieves a specific capacity of 75 mA h g^{-1}, even at a high current density of 10 A g^{-1}. Notably, CrGO also maintains a good specific capacity of 123 mA h g^{-1} after 1000 cycles at a current density of 1 A g^{-1}, with a capacity retention rate of 91.8%. This study highlights the potential for using coal-derived materials in the development of high-performance anode materials for SIBs, promoting the green and high-value utilization of coal.

1 Introduction

The overuse and development of fossil fuels, including coal, have caused significant global environmental issues.[1] Against this background, the increasing emphasis on environmental protection by human society, the extensive use of various smart devices, and the unprecedented development and utilization of new energy sources have raised higher demands for extensive energy storage solutions.[2] The growing need for large-scale clean energy production has driven the swift advancement of the secondary battery sector.[3] Lithium-ion batteries (LIBs) encounter uncertainties in further development due to the limited availability of lithium resources.[4] In contrast, sodium is abundant, widely distributed, and shares similar physico-chemical properties with lithium.[5] SIBs offer potential benefits compared to LIBs in safety and electrolyte conductivity. As a result, SIBs can act as an important supplement to LIBs.[6]

Currently, substantial advancements have been achieved in positive electrode materials for SIBs.[7] However, anode materials still encounter significant scientific challenges, particularly regarding capacity and cycling performance.[8,9] Among the developed anode materials, alloy materials and metal oxides, despite their high theoretical sodium storage capacities, suffer from poor cycling performance due to electrode material detachment caused by volume expansion during cycling.[10] Carbonaceous materials, known for their low cost, excellent structural stability, and large specific surface area (SSA), have emerged as the most widely used anode materials for SIBs.

Graphite, the anode material successfully used in industrial LIB applications, has a small interlayer spacing (0.3354 nm) making Na$^+$ intercalation/deintercalation difficult.[11–14] Hard carbon materials with larger interlayer spacing can meet sodium storage needs but are often derived from biomass,[15,16] resulting in low carbon yield, high preparation costs, and poor Na$^+$ intercalation/diffusion at high rates. This makes it difficult to achieve fast charging under the increasingly fast-paced living conditions.[17–19] Improving the capacitive adsorption behavior of materials can not only enhance Na storage capacity but also enable rapid Na$^+$ intercalation/deintercalation, thus meeting the need for fast charging.[20]

*a*State Key Laboratory of Coking Coal Resources Green Exploitation, China University of Mining and Technology, Xuzhou 221116, China

*b*School of Chemical Engineering and Technology, China University of Mining and Technology, Xuzhou 221116, China

*c*Henan Key Laboratory of Coal Green Conversion (Henan Polytechnic University), Jiaozuo 454000, China. E-mail: 18623855902@163.com

*d*Henan Polytechnic University – Ordos Institute of Clean Coal Development and Utilization, Ordos, 017000, China

Consequently, graphene materials with large SSA and numerous defects have attracted researchers' attention. Wang *et al.*[21] explored the sodium storage properties of reduced graphene oxide and discovered that it demonstrates high capacity and prolonged cycling stability at elevated current densities, attaining a reversible capacity of 174.3 mA h g^{-1} at a current density of 40 mA g^{-1}. Subsequently, Malyi *et al.*[22] employed density functional theory to reveal that ideal graphene with intrinsic structure is not a promising SIBs anode materials, whereas graphene with vacancy defects is more conducive to sodium ion transport within the material, a conclusion also reached by Ramos *et al.*[23] Luo *et al.* studied the sodium storage performance of graphene nanosheets finding that their high SSA, numerous active sites, and large interlayer spacing confer excellent sodium ion storage capacity.[24] These studies indicate that graphene with abundant active sites and large interlayer spacing can enhance sodium storage capacity and enable rapid Na$^+$ intercalation/deintercalation.

The green conversion and high-value utilization of coal is a crucial direction for low-carbon development.[25] Coal is a plentiful resource characterized by its high carbon content, substantial carbon yield, and abundant three-dimensional macromolecular material with a layered aromatic structure akin to graphite. These attributes make it an ideal precursor for producing various carbonaceous materials.[19,26–29] The macromolecular aromatic structure of coal facilitates its graphitization at high temperatures, with extensive literature on coal graphitization.[25,28,30–32] The level of graphitization in coal-based graphite can exceed 90%, making it an excellent precursor for preparing graphene.[25,33–35] Hence, in this work, CG was prepared by using three different coalification levels of coal. Subsequently, CrGO with large interlayer spacing, interlayer crosslinked carbon skeleton, and oxygen-containing functional groups was prepared using an modified Hummers-high temperature thermal reduction method. The unique structure of CrGO provides favorable conditions for the electrochemical intercalation of Na$^+$, enhancing the reversible capacity, cycling performance, and rate performance of SIBs. Consequently, CrGO demonstrates an initial reversible capacity of up to 331 mA h g^{-1} at a current density of 0.03 A g^{-1} and a specific capacity of 75 mA h g^{-1} at a high current density of 10 A g^{-1}. Remarkably, CrGO also exhibits excellent cycling stability, retaining a specific capacity of 123 mA h g^{-1} after 1000 cycles at a current density of 1 A g^{-1}, with a capacity retention rate of 91.8%. This study serves as an important reference for exploring the green and high-value utilization of coal of different ranks and for developing high-performance SIBs anode materials (Fig. 1).

2 Materials and methods

2.1 Materials

Three types of coal-based graphite (CG, including Indonesian Lignite-based Graphite (ILG), Hequ Bituminous Coal-based Graphite (HBG), Fengfeng Anthracite-based Graphite (FAG)) are prepared using Indonesian Lignite (IL), Hequ Bituminous coal (HB), and Fengfeng Anthracite (FA) respectively. The raw coal is crushed and ball-milled, then sieved with a 200-mesh sieve to obtain the undersize coal powder for use. The industrial analysis and elemental analysis of the raw coal are shown in Table 1.

2.2 Preparation of CrGO

In previous studies, the preparation method, formation mechanism, and microstructure of CG have been thoroughly investigated.[25,29] Using an improved Hummers' method, coal-based graphene oxide (CGO) was synthesized, and CrGO was prepared using a high-temperature thermal reduction method. The steps of preparing CrGO are shown in Fig. 2. The specific process is as follows: Firstly, under mechanical stirring and an
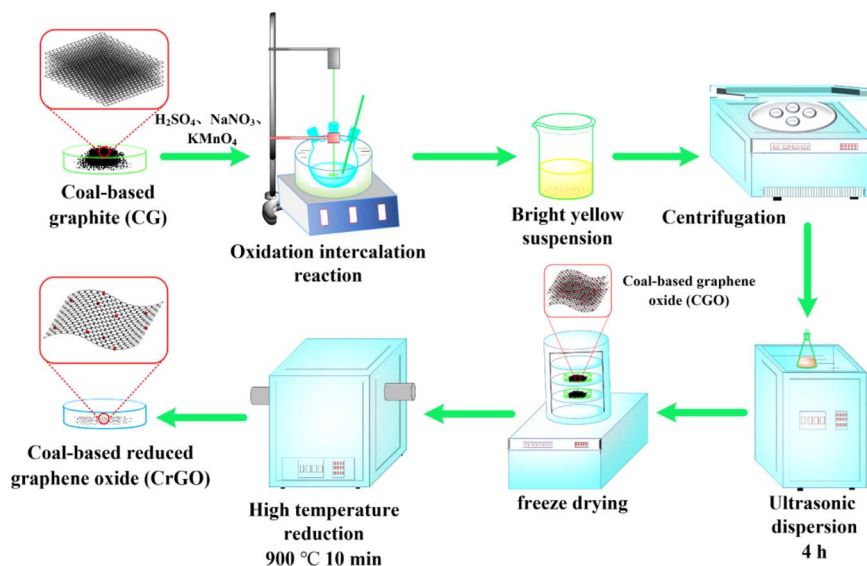

Fig. 1 Preparation flow chart of CrGO.

Table 1 Proximate analysis and ultimate analysis of raw coal[a]

Raw coal	Proximate analysis (wt%)				Ultimate analysis (wt%)				
	M_{ad}	A_d	V_{daf}	FC^*_{daf}	C_{daf}	H_{daf}	O_{daf}	N_{daf}	$S_{t,daf}$
IL	14.91	4.35	48.42	51.58	67.76	4.57	22.82	1.29	3.56
HB	2.83	19.89	41.26	58.74	73.82	4.94	19.41	1.09	0.74
FA	0.81	4.18	9.77	90.23	88.71	5.05	4.64	1.32	0.28

[a] ad: air-dried basis; d: dry basis; daf: dry and ash-free basis; *: by difference; wt%,: weight percentage.

ice-water bath, concentrated sulfuric acid (98%, 132 ml), coal-based graphite (3 g), $NaNO_3$ (3 g), and $KMnO_4$ (18 g) were sequentially added to a three-neck flask. After 6 hours of low-temperature reaction, the ice-water bath was quickly converted to a medium temperature reaction condition of 35 °C and maintained for 30 minutes. The reaction temperature was then gradually raised to 75 °C. At this point, while maintaining the temperature, we added 264 ml of deionized water was into the three-neck flask. Then it was followed by the dropwise addition of an appropriate amount of H_2O_2 until the suspension turned bright yellow. The bright yellow suspension was repeatedly centrifuged and washed with dilute hydrochloric acid and deionized water until neutral, resulting in a brown slurry. The brown slurry was then sonicated for 4 hours and freeze-dried to obtain a black powder, CGO. The CGO was placed in an alumina crucible at one end of a tube furnace, and the temperature was increased to 900 °C at a rate of 5 °C min^{-1} under a nitrogen atmosphere. The alumina crucible was then quickly pushed to the center of the furnace tube, reacted for 10 min, and then cooled to room temperature under natural conditions. And thus the corundum crucible was taken out, obtaining the black powder, *i.e.*, CrGO. Depending on the coal rank of the raw

materials, the samples were labeled as Indonesian Lignite-based reduced graphene oxide (ILrGO), Hequ Bituminous-based reduced graphene oxide (HBrGO), and Fengfeng Anthracite-based reduced graphene oxide (FArGO).

2.3 Material characterization

The elemental analysis of raw coal was performed using an macro elemental analyzer (vario MACRO cube, Germany). The micromorphology of CrGO was examined with FESEM (JEOL, JEM-2010, Japan) and HRTEM (JEOL, JEM-2100F). Raman and XRD (PANalytical Empyren) were utilized to determine the microstructural parameters, with measurements conducted on a Rigaku SmartLab with Cu-Kα radiation ($\lambda = 0.15406$ nm) and a Renishaw inVia (633 nm wavelength). XPS using a Thermo Escalab 250XI Scanning X-ray Microprobe was employed to analyze the surface chemical composition. Nitrogen adsorption–desorption at 77 K provided data on the SSA and pore structure.

2.4 Electrochemical characterization and cell assembly

For the electrochemical characterization, the rate and cycle performance measurements employing an the LAND CT2001A instruments (Wuhan, China). And the cyclic voltammetry (CV) measurement and EIS (between 100 kHz and 0.1 Hz) tests were conducted on the CHI 760E electrochemical workstation (Shanghai Chenhua Corp.).

For cell assembly, the required instruments include a vacuum glove box (Shanghai Mikrona, Supere), a sodium-ion battery sealer (Shenzhen Kejing MSK-110), and an electrode cutter (Shenzhen Kejing MSK-T10). The electrode sheet was prepared by coating the copper foil with active material, binder (PVDF), and conductive carbon black in the mass ratio of 8 : 1 : 1. The electrode sheets were 14 mm in diameter and each was
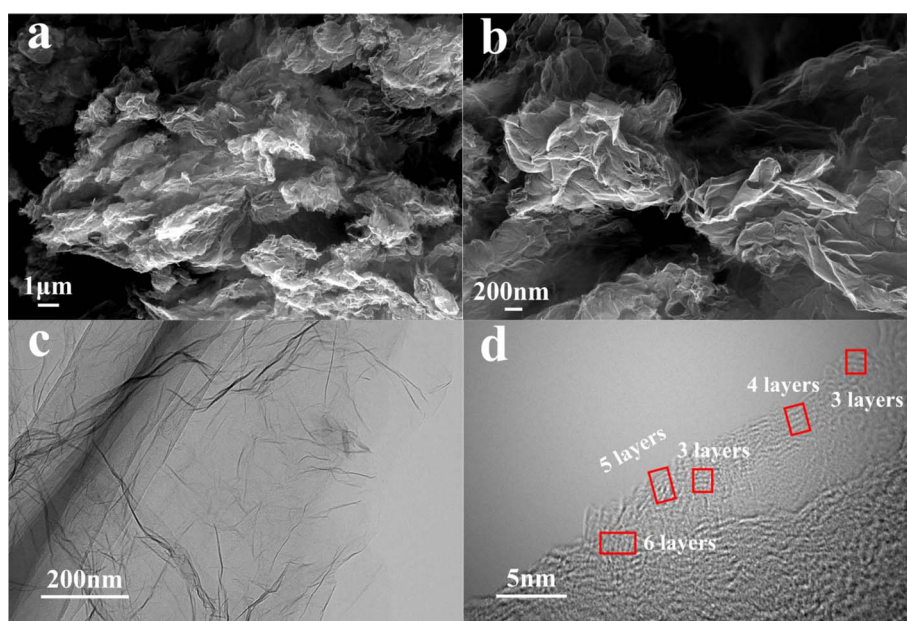

Fig. 2 SEM images (a and b), TEM images (c) and HRTEM images (d) of FArGO.

loaded with approximately 0.48 mg (0.31 mg cm^{-2}) of active substance.

3 Results and discussion

3.1 Microstructural analysis of CrGO

The microstructure of the CrGO variants (ILrGO, HBrGO, FArGO) was initially examined using scanning electron microscopy (SEM), as depicted in Fig. 2(a) and (b) and S1(a)–(d).† Using three types of coal graphitized at 2800 °C as raw materials, CGO was prepared through an improved Hummers' method, followed by ultrasonic exfoliation and high-temperature thermal reduction to obtain ILrGO (Fig. S1(a) and (b)†), HBrGO (Fig. S1(c) and (d)†), and FArGO (Fig. 2(a) and (b)). All samples exhibit a thin, layered structure akin to graphene prepared from natural flake graphite.[36]

TEM and HRTEM were utilized to further investigate the interlayer spacing and microstructure of ILrGO, HBrGO, and FArGO. As shown in Fig. 2(c) and (d) and S1(e)–(h),† all three CrGOs exhibit a transparent and wrinkled sheet-like morphology, indicating that the graphene layers were successfully exfoliated from coal-based graphite. The differences among these materials are that ILrGO (Fig. S1(e) and (f)†) has thicker layers with about 4–9 stacked graphene layers, HBrGO (Fig. S1(g) and (h)†) has slightly more layers than FArGO, with about 5–7 stacked graphene layers, while FArGO has fewer layers, with about 3–5 stacked graphene layers (Fig. 2(c) and (d)), consistent with the TEM results. The average interlayer spacing of ILrGO, HBrGO, and FArGO, calculated from lattice fringes, was 0.358, 0.367, and 0.375 nm. These values are significantly larger than the graphite interlayer spacing of 0.335 nm, indicating that the distance between the graphite layers was effectively expanded during the preparation of CrGO. The layered structure of CrGO facilitates rapid penetration of the electrolyte, providing wide diffusion channels for Na$^+$ to intercalate into the electrode material.

XRD and Raman were used to characterize ILG, HBG, FAG, ILrGO, HBrGO and FArGO elucidating the structural changes during the exfoliation process of CrGO. As shown in Fig. S2,† the XRD patterns of CG (ILG, HBG, and FAG) obtained after graphitization at 2800 °C, exhibit an unusually sharp (002) crystal plane diffraction peak at ~26.5°, a distinct (004) crystal plane diffraction peak at ~54.54°, and graphite's three-dimensional characteristic diffraction peaks at ~42.4°, ~44.5°, and ~77.4° for (100), (101), and (110) planes, respectively.[28] The degree of graphitization of the ILG, HBG and FAG prepared in this study was calculated to be 87.4%, 90.1% and 95.3%, respectively, with a graphite interlayer spacing of ~0.336 nm, indicating that anthracite is more easily graphitized under the same conditions.

The XRD patterns of ILrGO, HBrGO and FArGO prepared from ILG, HBG, and FAG are shown in Fig. 3(a). All three materials exhibit two broad and wide graphene characteristic peaks, the (002) and (100) crystal planes. The (002) crystal plane diffraction peaks are located at ~25.0°, ~24.6°, and ~24.1°, respectively. As the degree of coalification increases, the (002) peak shifts to smaller angles, indicating that the interlayer

spacing of FArGO is larger. The calculated interlayer spacings are ~0.359, ~0.366, and ~0.376 nm, which are roughly consistent with the interlayer spacings calculated from lattice fringes. This suggests that during the preparation of CrGO, the van der Waals forces holding the graphite layers together were entirely broken, transforming the structure from the ordered state of graphite to a disordered amorphous state, resulting in more open graphite layers.

The Raman spectra of ILrGO, HBrGO, and FArGO are presented in Fig. 3(b). All three samples display two prominent peaks at approximately 1341 cm^{-1} and 1580 cm^{-1}, representing the D and G vibration peaks of the three types of CrGO, respectively. Typically, the degree of graphitization (or disorder) can be assessed by the intensity ratio of the D and G vibration peaks (I_D/I_G).[37] The I_D/I_G values for ILrGO, HBrGO, and FArGO are 0.89, 0.91, and 0.97, respectively. This indicates that the graphite layers of CrGO were exfoliated into disordered graphene layers with significant defects, as defect-free graphene would not exhibit a D vibration peak. This is consistent with the evolution of the (002) peak in the XRD spectra. The presence of defects in ILrGO, HBrGO and FArGO creates numerous active sites for Na$^+$ storage, enhancing the material's ability to capture Na$^+$, thereby improving the reversible capacity of SIBs.

Next, the surface elemental composition of ILrGO, HBrGO, and FArGO was analyzed via XPS. As illustrated in Fig. 3(c), the XPS survey spectrum displays two significant peaks at 284.8 eV and 533.4 eV, corresponding to the C1s and O1s characteristic peaks, respectively. The oxygen content in CrGO is primarily related to the high-temperature reduction process, hence the oxygen content in ILrGO, HBrGO and FArGO is approximately the same, around 13% (at%). The high-resolution C1s spectrum of FArGO (Fig. 3(d)) can be deconvoluted into three distinct peaks, each representing different functional groups. The main peak at 284.7 eV, accounting for 47.5% (at%), corresponds to sp^2-hybridized C=C. The peaks at 286 eV and 288.8 eV, accounting for 36.7% and 15.8% (at%), respectively, correspond to C–O and C=O groups within the defective graphite lattice.[21,38] The small amount of oxygen-containing functional groups present on the surface of CrGO can maintain the interlayer distance at ~0.37 nm and chemically adsorb Na$^+$,[39] which positively affects the reversible capacity of SIBs.

Given the different degrees of graphene layer exfoliation in ILrGO, HBrGO and FArGO, their SSA and pore structures also vary. N$_2$ adsorption and desorption tests were conducted on ILrGO, HBrGO and FArGO at 77 K to analyze the SSA and pore structures of the materials, showing that the SSA of ILrGO, HBrGO and FArGO varys according to the coalification degree of the raw coal, being 399, 412, and 474 m^2 g^{-1}, respectively. The pore structure parameters are presented in Table S1.† The adsorption isotherms of ILrGO, HBrGO, and FArGO, shown in Fig. 3(e), belong to type IV isotherms according to the IUPAC classification. These isotherms exhibit H3-type hysteresis loops with the relative pressure range between 0.45 and 0.99, indicating that ILrGO, HBrGO, and FArGO possess typical mesoporous structures. Fig. 3(f) shows that the pore sizes of ILrGO, HBrGO and FArGO are mainly between 2 and 30 nm, with the corresponding average pore sizes being 9.12 nm (ILrGO),
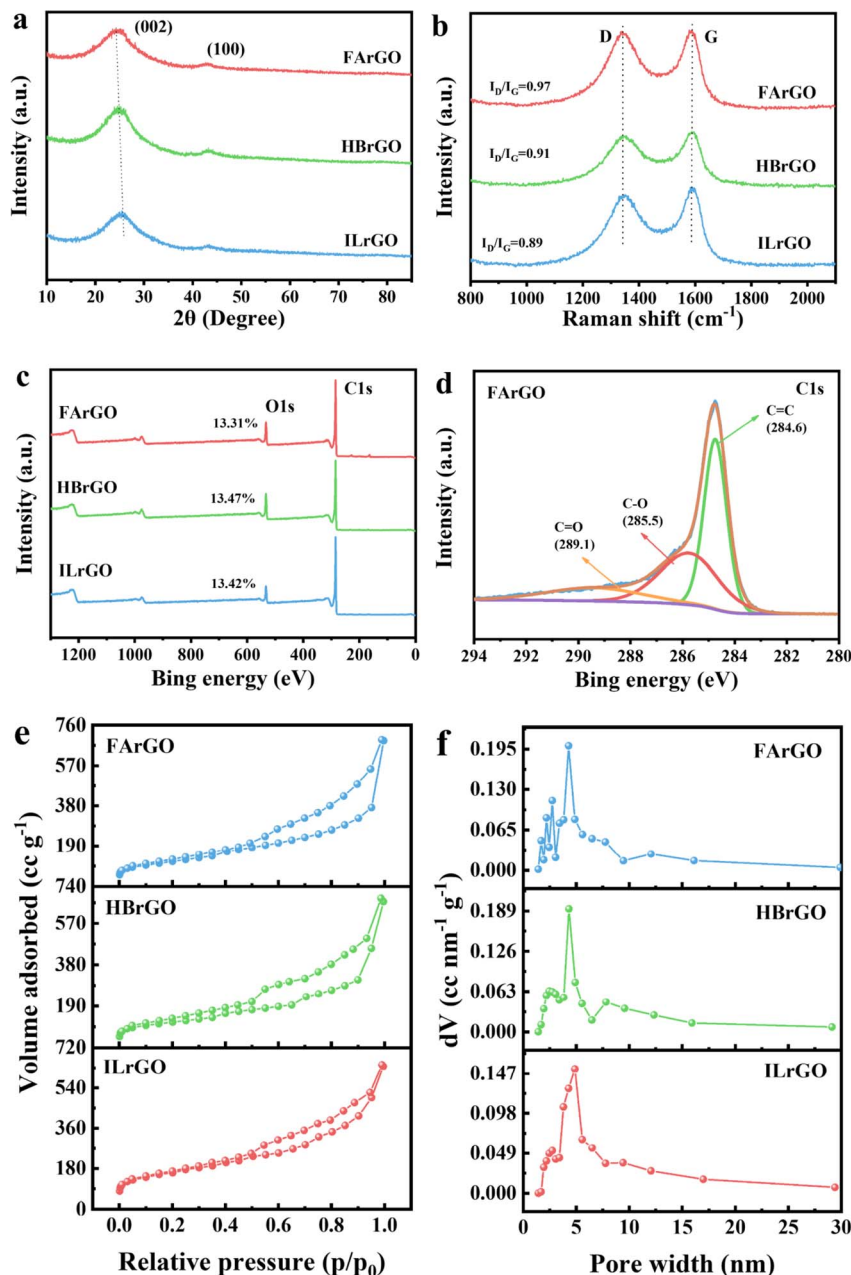
Fig. 3 The XRD (a) images of ILrGO, HBrGO and FArGO, Raman (b) images of ILrGO, HBrGO and FArGO, XPS survey spectrum of ILrGO, HBrGO, FArGO (c) and high-resolution C1s spectrum of FArGO (d), nitrogen adsorption and desorption isotherms (e) and pore size distribution images (f) of ILrGO, HBrGO and FArGO.

9.90 nm (HBrGO) and 10.21 nm (FArGO), indicating that coal-based reduced graphene oxide ILrGO, HBrGO and FArGO have abundant mesopores. The mesoporous structure of coal-based reduced graphene oxide enhances electrolyte penetration on the surface of the electrode material, shortens the Na^+ diffusion distance, and promotes charge transfer.

3.2 Electrochemical performance of the CrGO

The first three CV curves of ILrGO, HBrGO and FArGO are shown in Fig. 4(a) and S3(a) and (b).† The first CV curves of the three electrodes all show a large and broad cathodic reduction peak around 1 V and 0.5 V. This represents the decomposition of the electrolyte and the formation of the solid electrolyte interphase (SEI),[40] consistent with the irreversible discharge plateau in the first discharge curve. In subsequent cycles, these peaks no longer appear, indicating a stable SEI formed in the first cycle. The shapes of the subsequent two CV cycle curves exhibit minimal change and significant overlap, suggesting that the irreversible capacity primarily occurs in the first cycle. The weak anodic oxidation at high potentials and the rectangular CV curves of these materials indicate that a significant portion of the sodium storage capacity is attributed to the capacitive control process.[41]

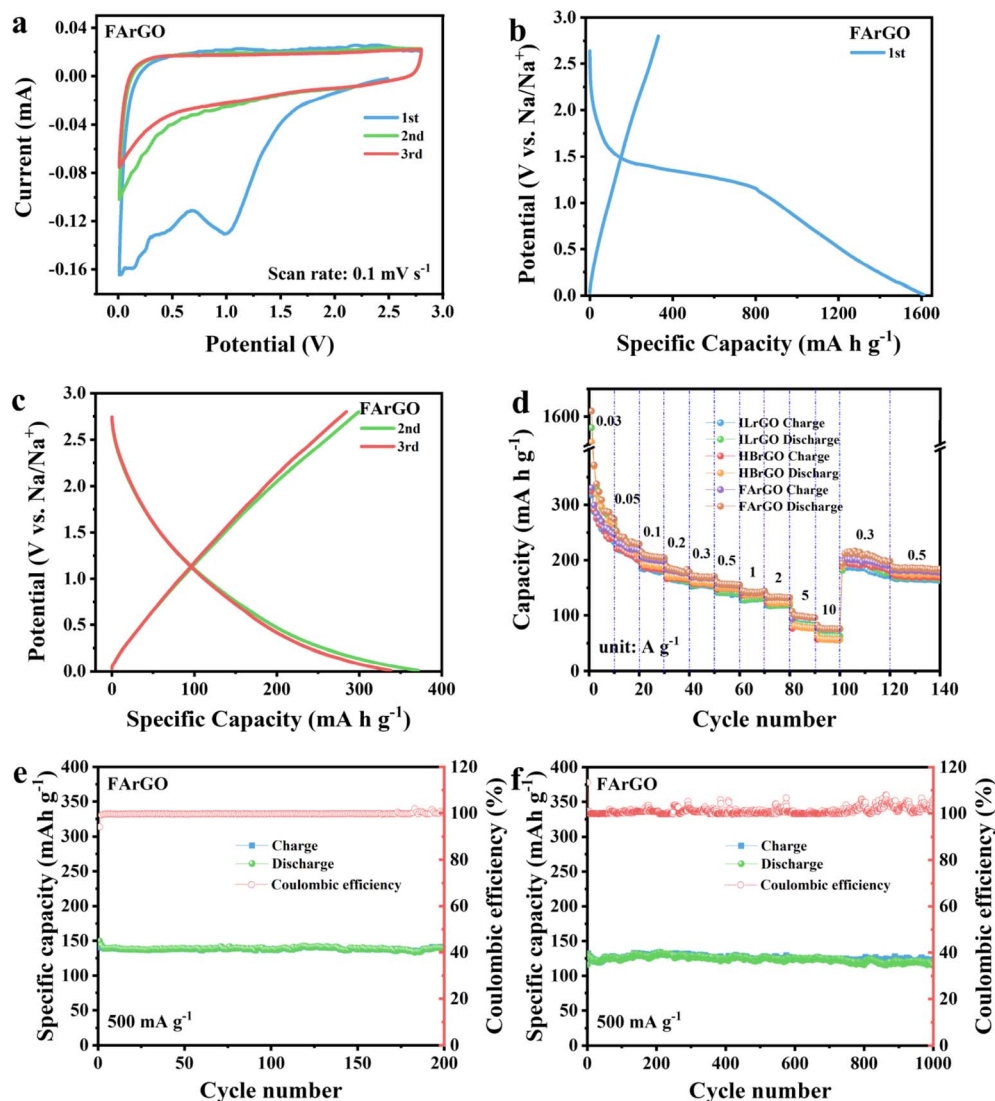Galvanostatic charge–discharge tests were conducted on CrGO (ILrGO, HBrGO and FArGO) electrode materials.

Fig. 4 The first three CV curves of FArGO (a), first three charge/discharge curves of FArGO (b and c), rate performance (d) of ILrGO, HBrGO, and FArGO, cycling stability of FArGO at 0.5 and 1 A g^{-1}.

Fig. S3(c)–(f)† and 4(b) and (c) show the first three charge–discharge curves of ILrGO (Fig. S3(c)†), HBrGO (Fig. S3(e)†) and FArGO (Fig. 4(b)) measured at a current density of 30 mA g^{-1} in 2.8–0.01 V, which represents the typical charge–discharge behavior of graphene materials for sodium storage.[21] As shown in the figures, the first reversible capacities of the three electrodes increase with the degree of coalification of the raw coal, being 312, 324, and 331 mA h g^{-1}. The initial coulombic efficiencies are relatively low, at 20.1%, 20.8%, and 20.6%, respectively. The first discharge curves of the three electrode materials show a significant discharge plateau around 1.5 V, while no corresponding charging plateau is observed in the first charge process. This discharge plateau corresponds to a large irreversible capacity in the first cycle. The main reason for this is that the large SSA causes the electrolyte to decompose on the electrode material surface and form SEI during the first discharge process, consuming a substantial amount of electrolyte. Fig. S3(d) and (f)† show that starting from the second

cycle, the coulombic efficiencies of sodium-ion batteries with ILrGO (Fig. S3(d)†), HBrGO (Fig. S3(f)†) and FArGO (Fig. 4(c)) increase to 77%, 75%, and 79%, respectively, and gradually approach 100% in subsequent cycles. The second discharge curves of ILrGO, HBrGO and FArGO can be distinctly divided into two stages: (1) a monotonically sloping voltage curve between 2.8–0.3 V, and (2) a sloping voltage plateau between 0.3 and 0.01 V.[12] Recent studies on Na storage in carbon materials[14,42,43] suggest that the monotonically sloping voltage curve in the high voltage region (>0.3 V) corresponds to the adsorption behavior of Na$^+$ at large interlayer distances (>0.4 nm) and defect sites (edges, heteroatoms, *etc.*), indicative of a surface capacitive adsorption process. The region of low voltage plateau (0.3–0.01 V) likely represents the insertion of Na$^+$ into graphene layers and nanopores, which is a diffusion-controlled process.[44] Therefore, the sodium storage mechanisms of ILrGO, HBrGO, and FArGO involve both surface diffusion-controlled processes and capacitive-induced processes.

The rate performance of CrGO (ILrGO, HBrGO, and FArGO) measured under different current densities is illustrated in Fig. 4(d). At the same current density, the reversible capacities of the three electrodes increase with the degree of coalification of the raw coal and the reduction in graphene layer stacks. The stable reversible capacities of FArGO at current densities of 0.03, 0.05, 0.1, 0.2, 0.3, 0.5, 1, and 2 A g^{-1} are 248, 218, 198, 175, 169, 155, 144, and 132 mA h g^{-1}, respectively. At elevated current densities of 5 and 10 A g^{-1}, FArGO maintains high reversible sodium storage capacities of 96 and 75 mA h g^{-1}, respectively, showcasing outstanding rate performance. When the current density is reduced to 0.03 and 0.05 A g^{-1}, the reversible capacities rebound to 199 and 182 mA h g^{-1}. Compared to the reversible capacity before the increase in current (248 mA h g^{-1}), the capacity retention rates are 80% and 73%, respectively, indicating that FArGO has good structural stability. Compared with FArGO, the reversible sodium storage capacities of ILrGO and HBrGO are lower at the same current density due to their thicker graphene layer stacks, smaller SSA and pore volumes, and lower defect degrees. The specific reversible capacities of the three electrodes at different current densities are shown in Table 2.

The long-term cycling tests of ILrGO, HBrGO and FArGO are shown in Fig. S3(g)–(j)† and 4(e) and (f). After the rate performance tests on the same battery, the electrodes ILrGO (Fig. S3(g)†), HBrGO (Fig. S3(i)†), and FArGO (Fig. 4(e)) were tested for 200 cycles at a current density of 0.5 A g^{-1}. Their initial reversible capacities were 124, 131, and 141 mA h g^{-1}, respectively. After 200 cycles, the reversible capacities were at 121, 130, and 140 mA h g^{-1}, showing almost no change, with coulombic efficiencies close to 100%. As shown in Fig. S3(h) and (j)† and 4(f), a new battery was activated at a current density of 0.1 A g^{-1} for 10 cycles, followed by 1000 cycles at a current density of 1 A g^{-1} for the electrodes ILrGO (Fig. S3(h)†), HBrGO (Fig S3(j)†) and FArGO (Fig. 4(f)). Their initial reversible capacities were 114, 122, and 132 mA h g^{-1}, respectively. After 1000 cycles, the reversible capacities were 105, 114, and 123 mA h g^{-1}, with capacity retention rates of 92.1%, 93.4%, and 91.8%, respectively. This demonstrates the outstanding cycling stability of coal-based reduced graphene oxide.

3.3 Sodium storage mechanism of CrGO

Further studies on sodium storage behavior were conducted using FArGO, the CrGO with the better sodium storage performance. To further verify the capacitive behavior and sodium storage performance of FArGO, CV curves at different scan rates ranging from 0.1 to 0.8 mV s^{-1} were analyzed, as shown in

Fig. 5(a). Generally, the scan rate (v) and peak current (i) satisfy the equation,[45] where a and b are adjustable parameters:

$$i = av^b \tag{1}$$

Taking the logarithm of both sides of eqn (1), we get:

$$\log i = b \log v + \log a \tag{2}$$

Substitute the measured peak current values and corresponding scan rates into eqn (2). By using software such as *Origin* to perform a linear fit on the logarithms of i and v in eqn (2), the value of b can be obtained (where b is the slope of the fitted line).

As illustrated in Fig. 5(b), the b values calculated from the fit of peak currents Peak2/Peak3 are 0.53/0.98, and those from the fit of peak currents Peak1/Peak4 are 0.75/0.87. This indicates that at low potentials, the discharge process involves both diffusion behavior and capacitive behavior. Since $b = 0.53$ is close to 0.5, the discharge process at low potentials is primarily diffusion-controlled, corresponding to the sloped discharge plateau observed at low potentials in the discharge curve. Conversely, the charging process is dominated by capacitive behavior with $b = 0.98$. At high potentials, both the charging and discharging processes involve a combination of diffusion and capacitive behaviors, with b values approaching 1. Therefore, the charging and discharging processes at high potentials are primarily dominated by capacitive behavior, corresponding to the sloped regions of the charge–discharge curves.

The calculation formula for the contribution of capacitive control to the total capacity of FArGO[41,44] is:

$$I = k_1 v + k_2 v^{1/2} \tag{3}$$

Dividing both sides of the formula by $v^{1/2}$ yields:

$$\frac{I}{v^{1/2}} = k_1 v^{1/2} + k_2 \tag{4}$$

In this formula, I represents the current at a specific voltage during a CV measurement at different scan rates; v is the voltage scan rate; k_1 and k_2 are adjustable parameters.

In the formula, $k_1 v$ and $k_2 v^{1/2}$ represent capacitive behavior and diffusion behavior, respectively. At a specific voltage, values for and can be derived by fitting the measured current I with the scan rate v. Connect many specific voltage points with the corresponding currents using a smooth curve, and perform a nonlinear fit. Then, integrate the area under the fitted curve

Table 2 Reversible capacity (mA h g^{-1}) of ILRGO, HBRGO and FARGO at different current densities (A g^{-1})

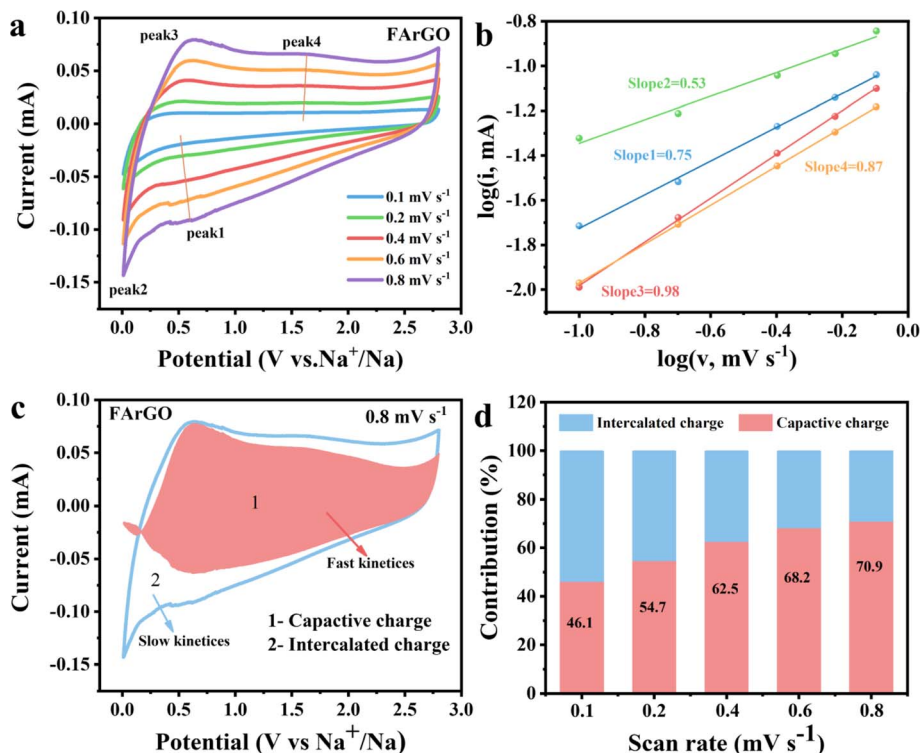| Samples	Current densities											
	0.03	0.05	0.1	0.2	0.3	0.5	1	2	5	10	0.03	0.05
ILrGO	233	199	183	160	152	139	130	119	83	63	187	169
HBrGO	238	202	182	165	156	148	137	122	77	59	192	174
FArGO	248	218	198	175	169	155	144	132	96	75	199	182

Fig. 5 The CV curves at different scan rate range between 0.1 and 0.8 mV s^{-1} of FArGO (a). The relationship between logarithm of peak current and logarithm of scan rates (b). The capacitive contribution in CV curves of FArGO at 0.8 mV s^{-1} (c). The capacitance contribution of FArGO at different scan rates (d).

and also integrate the area under the CV curve at specific voltage scan rates. The ratio of the area under the fitted curve to the area under the CV curve gives the rate of capacitive contribution at a specific scan rate.

The contribution rate of capacitive behavior reaches 70.9% at a scan rate of 0.8 mV s^{-1}, indicating that sodium ions adsorbed on the surface play a dominant role, as illustrated in Fig. 5(c). Further quantitative analysis of capacitive and diffusion behaviors is illustrated in Fig. 5(d). At a low scan rate of 0.1 mV s^{-1}, 46.1% of the sodium storage capacity is attributed to capacitive behavior. When the voltage scan rate is greater than 0.1 mV s^{-1}, the capacitance contribution rate surpasses 50%, highlighting that the capacitance-controlled capacity of FArGO is crucial at elevated rates (linked to higher scan speeds) and throughout extended cycling. This reasonably explains why FArGO electrodes exhibit outstanding rate performance and cycling stability: the main sodium storage capacity is contributed by capacitive behavior, and capacitive behavior reaction kinetics are fast and do not cause volume expansion of the material.

To evaluate the electrochemical kinetics of CrGO, the fresh cell, circulating cells with 10 cycles, and circulating cells with 1000 cycles of electrochemical impedance spectra (EIS) are given in Fig. 6. The equivalent circuit model (inset in Fig. 6(a)) is employed for fitting the resistance value of R_S, R_{SEI} and R_{CT}, in which R_s denotes the internal resistance, and R_{SEI} and R_{CT} correspond to SEI film resistance and charge-transfer resistance, respectively.[46–48] The Nyquist plots of the FArGO anode

before cycling consist of three parts: two depressed semicircles at the high and medium-frequency region and one inclined line at the low-frequency region. The depressed semicircle in the high-frequency region represents the solid electrolyte interface (SEI) film resistance (R_{SEI}: 528 Ω) with a parallel connection of capacitance (Q_{SEI}), attributing to the Na$^+$ migration through SEI film on the surface of the anode, showing the resistance to SEI film formation on the surface of FArGO. The semicircle at the medium-frequency region represents the charge transfer resistance (R_{CT}: 249 Ω) with the capacitance of the electrolyte and electrode interface (Q_d). The inclined line at the low-frequency region is assigned to the Warburg impedance (W), which is related to the Na$^+$ diffusion process. After the first cycle, a stable SEI film has formed, which can be also proved by galvanostatic charge/discharge profiles and CV curves, and thus the semicircle in the high-frequency region decreases rapidly. After 10 and 1000 cycles, the charge transfer resistance (R_{CT}) of FArGO are 492 Ω and 402 Ω, and the SEI membrane resistance (R_{SEI}) are 69 Ω and 54 Ω, respectively, indicating that the SEI membrane resistance (R_{SEI}) and charge transfer resistance (R_{CT}) of the FArGO electrode gradually decrease with the increase of the number of cycles, and the kinetics of the reaction is enhanced, and the kinetics of the reaction of the subsequent cycles are stabilized.[49,50]

Moreover, Fig. 6(b) presents the SEM image of the electrode after 1000 cycles, a loose structure with an ultra-thin rolling layer does not change compared with that of fresh anode (Fig. 2(a)). The electrodes after 1000 cycles still consisted of
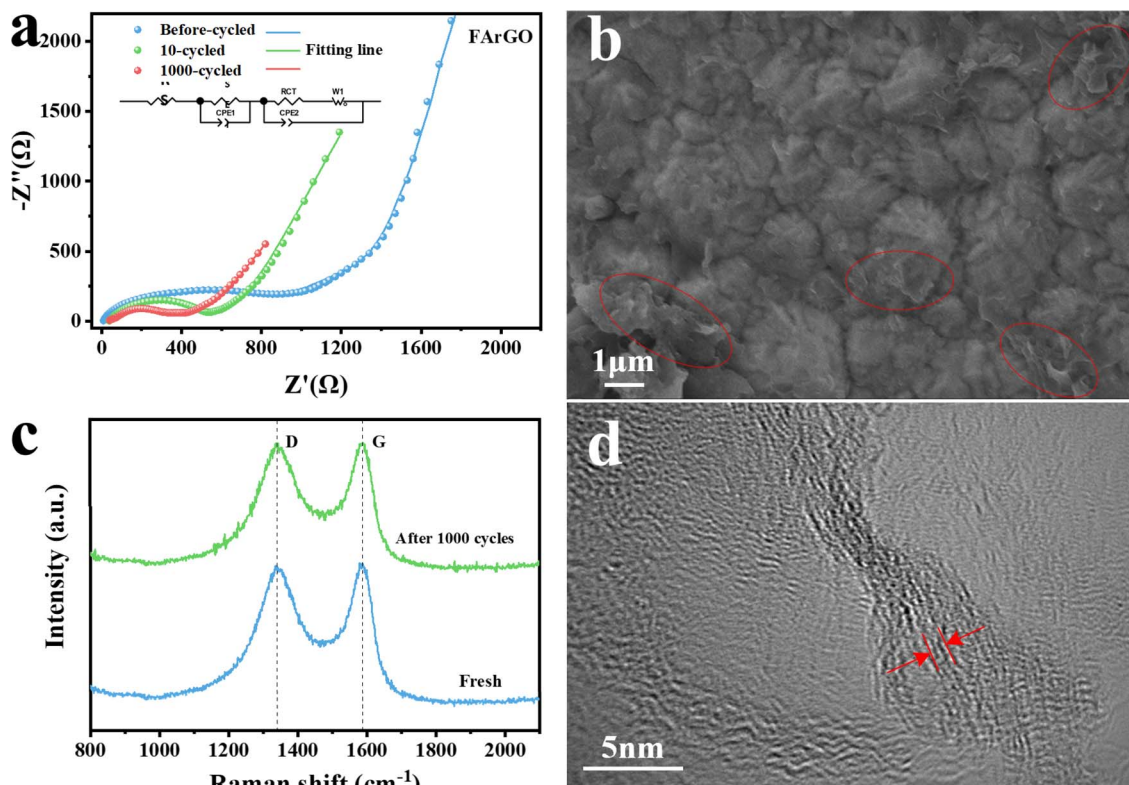
Fig. 6 The electrochemical impedance spectra (EIS) of FArGO (a), SEM image of FArGO after 1000 cycles (b), Raman spectrogram of fresh and FArGO after 1000 cycles (c), HRTEM images of the FArGO after 1000 cycles (d).

stochastically accumulated FArGO and the accompanying conductive additives and binders, whereas the wrinkles in the FArGO almost disappeared and the surface brightness of the electrodes decreased, suggesting that a thicker SEI was formed during the cycling process, proving that FArGO has excellent cycling stability.[51] In the meantime, the D and G-bands in the Raman spectra (Fig. 6(c)) of FArGO have not changed before and after cycling, leading to a very stable structure of FArGO during the charge/discharge process, and this phenomenon is favorable for the cycle and life-span performance of rechargeable SIBs.[52] The result of the HRTEM image in Fig. 6(d) demonstrates that the interlayer distance of FArGO increases to 0.381 nm after cycling, also indicating that FArGO has long cycling stability.

4   Conclusions

In summary, this work used CG from coals with different degrees of coalification as precursors to prepare CrGO with fewer graphene layers and numerous defects using an improved Hummers-high temperature thermal reduction method. The microstructural changes of CrGO with different coalification degrees were investigated. With increasing coalification, the interlayer spacing, SSA, and pore size increased, and the degree of graphene layer exfoliation improved. Anthracite-based reduced graphene oxide (FArGO) exhibited certain defects, providing fast diffusion channels for Na$^+$ storage and additional sodium storage sites. CrGO demonstrated high reversible

capacity, excellent rate performance, and stable cycling life. Specifically, FArGO exhibited an initial reversible capacity of 331 mA h g^{-1} at a current density of 30 mA g^{-1}. It achieved a reversible sodium storage capacity of 75 mA h g^{-1} at a high rate of 10 A g^{-1} and maintained a reversible sodium storage capacity of 140 mA h g^{-1} (with a capacity retention rate close to 100%) after 200 cycles at a current density of 500 mA g^{-1}. Furthermore, the FArGO electrode showed outstanding high-rate cycling performance, sustaining a reversible capacity of 123 mA h g^{-1} even after 1000 cycles at a current density of 1 A g^{-1}. Cyclic voltammetry analysis showed that the sodium storage behavior of the CrGO electrode was predominantly capacitive controlled with rapid diffusion kinetics.

Data availability

The data supporting this article have been included as part of the ESI.†

Author contributions

Lanhao Wang: investigation, methodology, data curation, writing – original draft, funding acquisition. Xiaodong Yu: conceptualization, supervision, funding acquisition. Zhendong Jiang: writing – review & editing, validation, project administration. Xuesheng Li: resources, data curation. Chuanxiang Zhang: validation, visualization, formal analysis.

Conflicts of interest

The authors declare that they have no known competing financial interests or personal relationships that could have appeared to influence the work reported in this paper.

Acknowledgements

References

1 Y. Li, Y.-S. Hu, X. Qi, et al., Advanced sodium-ion batteries using superior low cost pyrolyzed anthracite anode: towards practical applications, Energy Storage Mater., 2016, 5, 191–197.

2 Z. Lou, H. Wang, D. Wu, et al., Microcrystalline regulation of bituminous coal derived hard carbon by pre-oxidation strategy for improved sodium-ion storage, Fuel, 2022, 310, 122072.

3 K. Wu, X. W. Dou, X. X. Zhang, et al., The Sodium-Ion Battery: An Energy-Storage Technology for a Carbon-Neutral World, Engineering, 2023, 21, 36–38.

4 S. Q. Zhao, Z. Q. Guo, J. Yang, et al., Nanoengineering of Advanced Carbon Materials for Sodium-Ion Batteries, Small, 2021, 17(48), 2007431.

5 B. Swain, Recovery and recycling of lithium: a review, Sep. Purif. Technol., 2017, 172, 388–403.

6 T. W. Yu, G. H. Li, Y. Duan, et al., The research and industrialization progress and prospects of sodium ion battery, J. Alloys Compd., 2023, 958.

7 Y. J. Fang, L. F. Xiao, Z. X. Chen, et al., Recent Advances in Sodium-Ion Battery Materials, Electrochem. Energy Rev., 2018, 1(3), 294–323.

8 B.-Y. Wang, J.-L. Xia, X.-L. Dong, et al., Highly Purified Carbon Derived from Deashed Anthracite for Sodium-Ion Storage with Enhanced Capacity and Rate Performance, Energy Fuels, 2020, 34(12), 16831–16837.

9 X. Han, S. H. Zhou, H. Liu, et al., Noncrystalline Carbon Anodes for Advanced Sodium-Ion Storage, Small Methods, 2023, 7(3), 2201508.

10 B. Thangaraj, P. R. Solomon and J. Hassan, Nanocarbon in Sodium-ion Batteries - A Review. Part 1: Zero-dimensional Carbon Dots, ChemBioEng Rev., 2023, 10(5), 628–646.

11 Z. Jiang, B. Xing, X. Qu, et al., Anthracite-based expanded graphite as anode materials for sodium-ion batteries with exceptional sodium storage performances, J. Energy Storage, 2024, 83, 110667.

12 Y. Wen, K. He, Y. J. Zhu, et al., Expanded graphite as superior anode for sodium-ion batteries, Nat. Commun., 2014, 5, 10.

13 Y. L. Cao, L. F. Xiao, M. L. Sushko, et al., Sodium Ion Insertion in Hollow Carbon Nanowires for Battery Applications, Nano Lett., 2012, 12(7), 3783–3787.

14 C. Bommier, T. W. Surta, M. R. Dolgos, et al., New Mechanistic Insights on Na-Ion Storage in Nongraphitizable Carbon, Nano Lett., 2015, 15(9), 5888–5892.

15 M. D. Yan, Y. C. Qin, L. X. Wang, et al., Recent Advances in Biomass-Derived Carbon Materials for Sodium-Ion Energy Storage Devices, Nanomaterials, 2022, 12(6), 930.

16 S. Huang, X. Q. Qiu, C. W. Wang, et al., Biomass-derived carbon anodes for sodium-ion batteries, New Carbon Mater., 2023, 38(1), 40–72.

17 F. J. Wang, T. Y. Zhang and F. Ren, Insights into sodium-ion batteries through plateau and slope regions in cyclic voltammetry by tailoring bacterial cellulose precursors, Electrochim. Acta, 2023, 441, 141770.

18 Y. J. Zou, H. Li, K. Y. Qin, et al., Low-cost lignite-derived hard carbon for high-performance sodium-ion storage, J. Mater. Sci., 2020, 55(14), 5994–6004.

19 H. Lu, S. Sun, L. Xiao, et al., High-Capacity Hard Carbon Pyrolyzed from Subbituminous Coal as Anode for Sodium-Ion Batteries, ACS Appl. Energy Mater., 2019, 2(1), 729–735.

20 Y. Dong, X. J. Lin, D. K. Wang, et al., Modulating the defects of graphene blocks by ball-milling for ultrahigh gravimetric and volumetric performance and fast sodium storage, Energy Storage Mater., 2020, 30, 287–295.

21 Y.-X. Wang, S.-L. Chou, H.-K. Liu, et al., Reduced graphene oxide with superior cycling stability and rate capability for sodium storage, Carbon, 2013, 57, 202–208.

22 O. I. Malyi, K. Sopiha, V. V. Kulish, et al., A computational study of Na behavior on graphene, Appl. Surf. Sci., 2015, 333, 235–243.

23 A. Ramos, I. Cameán, N. Cuesta, et al., Is single layer graphene a promising anode for sodium-ion batteries?, Electrochim. Acta, 2015, 178, 392–397.

24 X. Luo, C. Yang, Y. Peng, et al., Graphene nanosheets, carbon nanotubes, graphite, and activated carbon as anode materials for sodium-ion batteries, J. Mater. Chem. A, 2015, 3(19), 10320–10326.

25 H. Zeng, B. Xing, Y. Cao, et al., Insight into the microstructural evolution of anthracite during carbonization-graphitization process from the perspective of materialization, Int. J. Min. Sci. Technol., 2022, 32, 1397–1406.

26 Z. Jiang, C. Zhang, X. Qu, et al., Humic acid resin-based amorphous porous carbon as high rate and cycle performance anode for sodium-ion batteries, Electrochim. Acta, 2021, 372, 137850.

27 Z. Jiang, Y. Zhao, W. Kang, et al., Anthracite-based Reduced Graphene Oxide/Antimony Composites as Anode Materials for High Performance Sodium Ion Batteries, J. Alloys Compd., 2022, 166631.

28 L. Tang, Q. Y. Mao, Z. H. You, et al., Catalytic graphitization in anthracite by reduced iron particles and investigating the mechanism of catalytic transformation via molecular dynamics, Carbon, 2022, 188, 336–348.

29 B. Xing, C. Zhang, Y. Cao, et al., Preparation of synthetic graphite from bituminous coal as anode materials for high

performance lithium-ion batteries, *Fuel Process. Technol.*, 2018, **172**, 162–171.

30 X. M. Zhang, S. Q. Wang, H. Chen, *et al.*, Observation of carbon nanostructure and evolution of chemical structure from coal to graphite by high temperature treatment, using componental determination, X-ray diffraction and high-resolution transmission electron microscope, *Fuel*, 2023, **332**, 126145.

31 M. S. Nyathi, C. B. Clifford and H. H. Schobert, Characterization of graphitic materials prepared from different rank Pennsylvania anthracites, *Fuel*, 2013, **114**, 244–250.

32 I. Camean, P. Lavela, J. L. Tirado, *et al.*, On the electrochemical performance of anthracite-based graphite materials as anodes in lithium-ion batteries, *Fuel*, 2010, **89**(5), 986–991.

33 R. Q. Li, Y. G. Tang, Q. L. Che, *et al.*, Effects of Coal Rank and Macerals on the Structure Characteristics of Coal-Based Graphene Materials from Anthracite in Qinshui Coalfield, *Minerals*, 2022, **12**(5), 588.

34 L. L. Sun, Z. B. Zhao, Y. Sun, *et al.*, Activated coal-based graphene with hierarchical porous structures for ultra-high energy density supercapacitors, *Diam. Relat. Mater.*, 2020, **106**, 8.

35 Q. Zhou, Z. B. Zhao, Y. T. Zhang, *et al.*, Graphene Sheets from Graphitized Anthracite Coal: Preparation, Decoration, and Application, *Energy Fuels*, 2012, **26**(8), 5186–5192.

36 X. Wang, G. Li, F. M. Hassan, *et al.*, Sulfur covalently bonded graphene with large capacity and high rate for high-performance sodium-ion batteries anodes, *Nano Energy*, 2015, **15**, 746–754.

37 M. Kang, H. Zhao, J. Ye, *et al.*, Adsorption dominant sodium storage in three-dimensional coal-based graphite microcrystal/graphene composites, *J. Mater. Chem. A*, 2019, **7**(13), 7565–7572.

38 Q. Zhou, Z. Zhao, Y. Zhang, *et al.*, Graphene Sheets from Graphitized Anthracite Coal: Preparation, Decoration, and Application, *Energy Fuels*, 2012, **26**, 5186–5192.

39 Y. W. Wang, N. Xiao, Z. Y. Wang, *et al.*, Rational design of high-performance sodium-ion battery anode by molecular engineering of coal tar pitch, *Chem. Eng. J.*, 2018, **342**, 52–60.

40 J. Abou-Rjeily, N. A. Laziz, C. Autret-Lambert, *et al.*, Towards valorizing natural coals in sodium-ion batteries: impact of coal rank on energy storage, *Sci. Rep.*, 2020, **10**(1), 15871.

41 D.-Y. Kim, O. L. Li and J. Kang, Maximizing the rate capability of carbon-based anode materials for sodium-ion batteries, *J. Power Sources*, 2021, **481**, 228973.

42 N. Sun, Z. R. X. Guan, Y. W. Liu, *et al.*, Extended "Adsorption-Insertion" Model: A New Insight into the Sodium Storage Mechanism of Hard Carbons, *Adv. Energy Mater.*, 2019, **9**(32), 14.

43 H. Y. Lu, F. X. Ai, Y. L. Jia, *et al.*, Exploring Sodium-Ion Storage Mechanism in Hard Carbons with Different Microstructure Prepared by Ball-Milling Method, *Small*, 2018, **14**(39), 8.

44 P. Lu, Y. Sun, H. Xiang, *et al.*, 3D Amorphous Carbon with Controlled Porous and Disordered Structures as a High-Rate Anode Material for Sodium-Ion Batteries, *Adv. Energy Mater.*, 2018, **8**(8), 1702434.

45 Q. Ren, Z. Shi, L. Yan, *et al.*, High-performance sodium-ion storage: multi-channel carbon nanofiber freestanding anode contrived via ingenious solvent-induced phase separation, *J. Mater. Chem. A*, 2020, **8**(38), 19898–19907.

46 Z. Xu, J. Wang, Z. Y. Guo, *et al.*, The Role of Hydrothermal Carbonization in Sustainable Sodium-Ion Battery Anodes, *Adv. Energy Mater.*, 2022, **12**(18), 2200208.

47 B. Quan, A. Jin, S. H. Yu, *et al.*, Solvothermal-Derived S-Doped Graphene as an Anode Material for Sodium-Ion Batteries, *Adv. Sci.*, 2018, **5**(5), 7.

48 N. Gupta and P. Bhattacharya, Microwave-plasma induced one-step synthesis of $Ni(PO_3)_2$ nanosphere-loaded bio-waste derived N, P co-doped carbon for an asymmetric supercapacitor with prolonged life, *J. Mater. Chem. C*, 2023, **11**(39), 13503–13517.

49 Q. Liu, R. G. Xu, D. B. Mu, *et al.*, Progress in electrolyte and interface of hard carbon and graphite anode for sodium-ion battery, *Carbon Energy*, 2022, **4**(3), 458–479.

50 C. Song, S. Li and Y. Bai, High-lattice-adapted surface modifying Na4MnV(PO4)3 for better sodium storage, *Nano Res.*, 2023, **17**(4), 2728–2735.

51 J. Zhang, D.-W. Wang, W. Lv, *et al.*, Achieving superb sodium storage performance on carbon anodes through an ether-derived solid electrolyte interphase, *Energy Environ. Sci.*, 2017, **10**(1), 370–376.

52 L. F. Zhou, Y. J. Gao, H. Gong, *et al.*, Application of an inorganic sulfur-modified expanded graphite anode for sodium storage at low temperatures, *Sustain. Energy Fuels*, 2021, **5**(20), 5160–5165.